UNIVERSITY OF BRISTOL

University of Bristol - Explore Bristol Research
General rights

CrossMark

X-Ray Jets in the High-redshift Quasars J1405+0415 and J1610+1811

Bradford Snios[1] , Daniel A. Schwartz[1] , Aneta Siemiginowska[1] , Małgosia Sobolewska[1] , Mark Birkinshaw[2] ,
C. C. Cheung[3] , Doug B. Gobeille[4], Herman L. Marshall[5] , Giulia Migliori[6,7] , John F. C. Wardle[8], and Diana M. Worrall[2]

[1] Center for Astrophysics | Harvard & Smithsonian, Cambridge, MA 02138, USA
[2] H.H. Wills Physics Laboratory, University of Bristol, Bristol BS8 1TL, UK
[3] Space Science Division, Naval Research Laboratory, Washington, DC 20375, USA
[4] Physics Department, University of Rhode Island, Kingston, RI 02881, USA
[5] Kavli Institute for Astrophysics and Space Research, Massachusetts Institute of Technology, Cambridge, MA 02139, USA
[6] Department of Physics and Astronomy, University of Bologna, Via Gobetti 93/2, I-40129 Bologna, Italy
[7] INAF-Institute of Radio Astronomy, Bologna, Via Gobetti 101, I-40129 Bologna, Italy
[8] Physics Department, Brandeis University, Waltham, MA 02454, USA

Abstract

We investigate Chandra X-ray observations of the radio-loud quasars J1405+0415 and J1610+1811 at redshifts $z = 3.215$ and $z = 3.122$, respectively, for evidence of extended X-ray emission. Observations totalling 95 ks per target are combined, and X-ray jets that are spatially coincident with known radio features are detected at a greater than 4σ significance. Hardness ratios and emission spectra are determined for all X-ray features, and X-ray fluxes and luminosities are measured. Jet-to-core X-ray flux ratios are estimated for each system, and the ratios are consistent with those observed for nearby and more distant jet systems, although the spread in the parameter is large. These results suggest that to first order the X-ray jet emission mechanisms are redshift invariant. In addition to the extended emission analysis, incorporating also archival data from Swift, we examined the properties of a decline in the Chandra flux from the active galactic nucleus (AGN) of J1610+1811 observed between 2018 and 2021. We conclude that the variability is most likely due to a flaring event that occurred between the years 2017 and 2018 and originated from either the AGN or the inner jet region.

Unified Astronomy Thesaurus concepts: High-redshift galaxies (734); Jets (870); X-ray active galactic nuclei (2035)

Supporting material: machine-readable table

1. Introduction

Jetted outflows from active galactic nuclei (AGN) are a well-established phenomenon in extragalactic radio sources (e.g., Blandford & Rees 1974). Jets may propagate with bulk relativistic motion over kiloparsec-scale distances and transport significant energy from the supermassive black hole (SMBH) to the surrounding intercluster medium (Begelman et al. 1984; Bridle & Perley 1984). The power of a jet is dictated by the accretion of gas onto the SMBH (Schwartz et al. 2006a), while the jet is responsible for feedback processes that dictate the gas cooling rate (Bîrzan et al. 2004; McNamara & Nulsen 2012). Thus, a jet is inexorably linked to the evolution of its host galaxy and cluster, motivating in-depth studies of these exotic objects.

In studying jets, X-ray observations provide the best probe for sites of particle acceleration as high-energy radiation is generally produced by more energetic particles (Harris & Krawczynski 2002). The lifetime of these high-energy particles makes X-ray studies uniquely capable of discriminating between various jet emission mechanisms (Heavens & Meisenheimer 1987; Dermer & Atoyan 2002), although the origin of the X-ray jet emission is not uniquely defined. Additionally, the relative importance of different X-ray emission mechanisms may vary as a function of redshift. For

example, inverse Compton upscattering of the cosmic microwave background radiation (IC/CMB) is predicted to be the dominant X-ray emission mechanism for jets at high redshifts ($z > 3$) as the cosmological diminution of surface brightness by the factor $(1 + z)^{-4}$ is offset by the $(1 + z)^4$ increase in the CMB energy density (e.g., Schwartz et al. 2020).

Previous Chandra observations have successfully resolved X-rays jets in radio-loud quasars up to $z = 6.1$ (e.g., Siemiginowska et al. 2003; Cheung 2006, 2012; McKeough et al. 2016; Simionescu 2016; Ighina et al. 2022), though X-ray jets at $z > 3$ remain vastly undersampled in comparison to nearby sources (Worrall et al. 2020). It is consequently difficult to determine population trends of jets over a broad redshift range, making each detection of a high-redshift jet a significant discovery. Furthermore, understanding how jets in radio-loud quasars work and impact their environment is of particular importance given the recent discoveries of radio-loud quasars at the highest redshifts (e.g., Bañados et al. 2018, 2021).

Recent efforts have been made toward identifying more high-redshift jet candidates through the use of short, "snapshot" X-ray observations of radio-loud quasars (Schwartz et al. 2020; Snios et al. 2021), in which flux and morphological analyses are utilized to assess the presence of extended X-rays and the likelihood that said emission is from a jet. These surveys subsequently compile a sample of candidate X-ray jets at high redshifts that are ideal for follow-up morphological and spectroscopic studies. Thus, our focus for this paper is to investigate follow-up X-ray observations of the quasars J1405 +0415 and J1610+1811 to confirm at high probability the

Table 1
Chandra Observations and X-Ray Photometry of Each Quasar

Object	z[a]	ObsID[b]	Observation Date	t_{exp}[c] (ks)	X-Ray Counts 0.5–7.0 keV	0.5–2.0 keV	2.0–7.0 keV	HR[d]
J1405+0415	3.215	20408	2018 May 08	9.57	$286.8^{+15.7}_{-17.4}$	$165.4^{+11.5}_{-13.8}$	$121.3^{+9.9}_{-11.6}$	$-0.15^{+0.06}_{-0.06}$
...	...	23649	2021 Apr 29	15.28	$396.7^{+18.8}_{-20.3}$	$211.3^{+13.4}_{-15.2}$	$185.4^{+12.4}_{-14.2}$	$-0.07^{+0.05}_{-0.05}$
...	...	24316	2021 Apr 18	14.33	$365.7^{+17.9}_{-19.6}$	$193.3^{+12.8}_{-14.6}$	$172.4^{+12.0}_{-13.7}$	$-0.06^{+0.05}_{-0.05}$
...	...	24317	2021 Apr 21	24.79	$620.6^{+23.1}_{-25.7}$	$316.3^{+16.2}_{-18.8}$	$304.3^{+16.6}_{-17.1}$	$-0.02^{+0.04}_{-0.04}$
...	...	25011	2021 Apr 19	20.03	$477.6^{+20.5}_{-22.3}$	$248.3^{+14.3}_{-16.7}$	$229.3^{+14.5}_{-14.9}$	$-0.04^{+0.04}_{-0.05}$
...	...	25014	2021 May 01	13.37	$353.7^{+17.6}_{-19.4}$	$180.3^{+12.4}_{-14.1}$	$173.3^{+12.5}_{-13.2}$	$-0.02^{+0.06}_{-0.05}$
J1610+1811	3.122	20410	2018 May 24	9.09	$395.7^{+19.8}_{-19.4}$	$239.4^{+14.2}_{-16.4}$	$156.3^{+11.4}_{-12.9}$	$-0.21^{+0.05}_{-0.05}$
...	...	23648	2021 May 04	26.69	$633.3^{+24.3}_{-25.0}$	$339.1^{+15.8}_{-20.1}$	$294.2^{+16.5}_{-16.8}$	$-0.07^{+0.04}_{-0.04}$
...	...	24486	2021 May 12	14.33	$331.6^{+15.6}_{-20.2}$	$165.3^{+11.9}_{-13.5}$	$166.3^{+12.3}_{-12.9}$	$0.00^{+0.06}_{-0.05}$
...	...	24487	2021 May 29	28.59	$793.5^{+26.6}_{-28.3}$	$447.2^{+22.1}_{-19.6}$	$346.3^{+18.0}_{-18.2}$	$-0.13^{+0.03}_{-0.03}$
...	...	25035	2021 May 12	14.71	$365.6^{+17.6}_{-19.9}$	$203.3^{+13.0}_{-15.1}$	$162.3^{+11.7}_{-13.2}$	$-0.11^{+0.05}_{-0.05}$

Notes.
[a] Redshift measurements from Sowards-Emmerd et al. (2005) and Pâris et al. (2018).
[b] Observations performed using Chandra ACIS-S instrument with the aimpoint on the S3 chip.
[c] Exposure time.
[d] Hardness ratio (HR) for each observation. HR is defined as $\frac{H-S}{H+S}$, where H and S correspond to the hard (2.0–7.0 keV) and soft (0.5–2.0 keV) bands, respectively. Errors for the X-ray counts and the HR were computed to 1σ based on the method described in Park et al. (2006).

candidate jets inferred from previous X-ray studies (Schwartz et al. 2020; Snios et al. 2021).

This paper is one in a series on Chandra observations of radio-luminous quasars at $3.0 < z < 4.0$ with evidence of extended X-rays (Schwartz et al. 2020; Snios et al. 2021), and the remainder of the paper is arranged as follows. Section 2 outlines the X-ray data reduction and image alignment. Section 3 discusses the X-ray hardness ratio (HR) and spectroscopic analysis of each AGN. Section 4 details the X-ray morphological analysis utilized in our study, which includes deconvolved images of the systems. Section 5 describes the measured physical properties of the extended X-ray emission. Section 6 highlights variations in brightness detected from J1610+1811 and discusses possible physical origins for this behavior, and our concluding remarks are provided in Section 7.

For this paper, we adopted the cosmological parameters $H_0 = 70 \text{ km s}^{-1} \text{ Mpc}^{-1}$, $\Omega_\Lambda = 0.7$, and $\Omega_M = 0.3$ (Planck Collaboration et al. 2016). All reported measurement errors are at a 1σ confidence level, unless otherwise stated.

2. Data Reduction

Observations of the quasars J1405+0415 (J2000: 14:05:01.120, +04:15:35.82) and J1610+1811 (J2000: 16:10:05.289, +18:11:43.47) were performed with Chandra using the Advanced CCD Imaging Spectrometer (ACIS) with the aimpoint on the S3 chip. Coordinates for the sources were based on Very Large Array (VLA) centroid positions reported in Gobeille et al. (2014). All observations were configured in the 1/4 subarray timed to minimize pileup from the AGN core, and we verified that no pileup was detected from the cores. The exposure mode was set to vfaint telemetry, and roll direction was oriented perpendicular to the jet to avoid contamination along any possible extended X-ray jet emission from either readout streaks or point-spread function (PSF) artifact effects. The images were reprocessed using the default level 2 data products from the Chandra data processing pipeline together

with the software analysis package CIAOv4.13 with CALDBv4.9.6. A complete list of the observations is shown in Table 1. In total, the coadded exposure times are 97.4 and 93.4 ks for J1405+0415 and J1610+1811, respectively, which is a factor of 10 improvement in exposure over previous X-ray analyses (Schwartz et al. 2020; Snios et al. 2021).

Radio observations of J1405+0415 and J1610+1811 previously resolved subarcsecond radio features at arcsecond-scale separations from the core (Figure 1; Snios et al. 2021). As these angular scales are comparable to the 0″.4 nominal PSF FWHM of Chandra, careful astrometric alignment of the X-ray observations is required in order to analyze extended X-ray features. We therefore applied the two-dimensional cross-correlation alignment method described in Snios et al. (2018), which we briefly summarize below.

Each observation of a given quasar was spatially binned over the 0.5–7.0 keV band, and a rectangular region of $10'' \times 10''$ centered on the AGN was extracted for each epoch. The longest exposure observation of each source was treated as the reference image, and a two-dimensional cross-correlation function was calculated between said reference image and each remaining epoch. The cross-correlation function was fit with a two-dimensional Lorentzian profile to determine their relative offset, and the offset was corrected using the CIAO routine wcs_update. We found the average astrometric corrections to be on subarcsecond scales for both sources, which is consistent with the 90% absolute position uncertainty of 0″.8 for Chandra. We repeated the cross-correlation analysis on the shifted images and found all to agree within an average $\Delta x = 0''.112$ and $\Delta y = 0''.113$, or ~1/4 of an ACIS pixel. These results reinforce that our image alignment is at a sufficient level of precision for our extended emission analysis. The coadded X-ray image for each source is shown in Figure 1. Consistent with Snios et al. (2021), the X-ray and radio observations were aligned based on the centroid position of the core where the centroid was measured using the dmstat routine in CIAO. The X-ray observation coordinates were shifted with wcs_update to match the radio data.
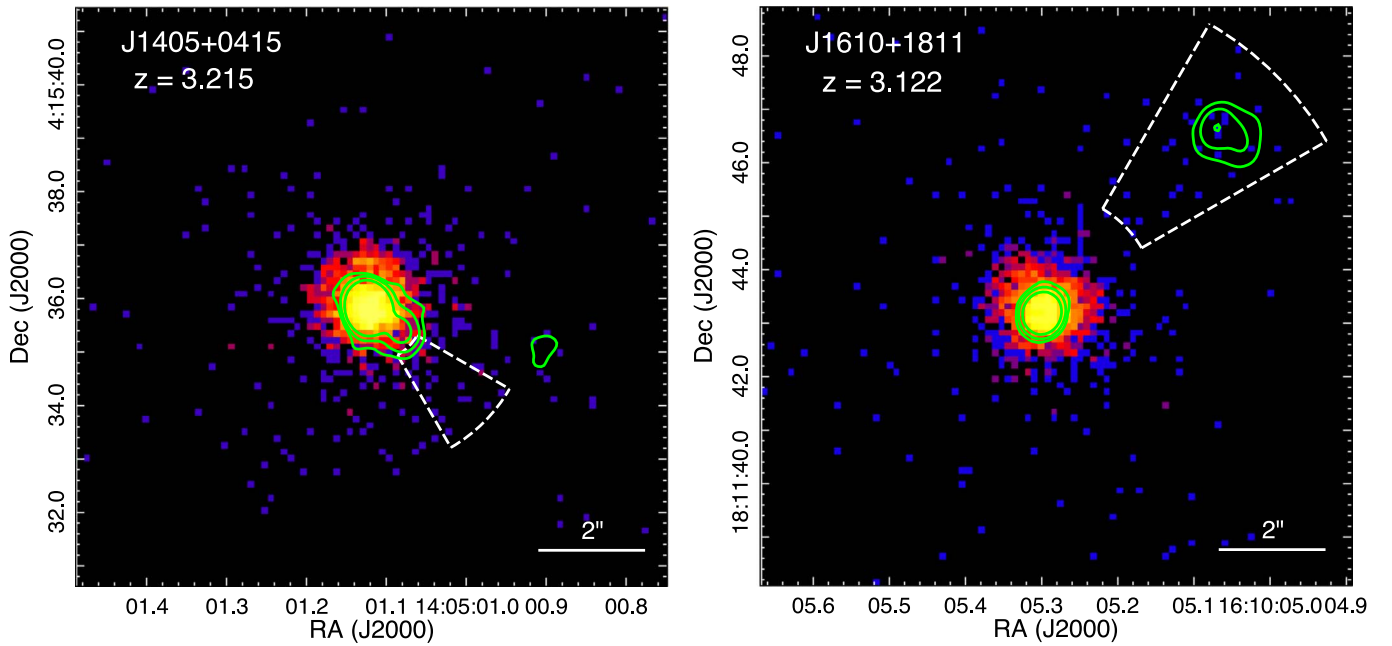
Figure 1. Coadded 0.5–7.0 keV images of J1405+0415 (left) and J1610+1811 (right), where the pixel size is $0\overset{''}{.}125$. Each image includes all relevant observations from Table 1 after performing astrometric alignments. The X-ray images are overlaid with radio map contours (green) from VLA observed at 6.2 GHz as well as sectors where extended X-rays are detected (white, dashed) based on our analysis in Section 4.

3. AGN X-Ray Analysis

3.1. Hardness Ratios

The X-ray count rate of each quasar in our sample was measured using a $1\overset{''}{.}5$ radius circular region centered on the source. A background annular region with an inner radius of $15''$ and an outer radius of $30''$ was also defined, and we verified that the regions were devoid of background point sources. The background-subtracted counts for each source over the 0.5–2.0 (soft), 2.0–7.0 (hard), and 0.5–7.0 keV (broad) energy bands are reported in Table 1.

We additionally measured the HR for each observation using our defined soft and hard bands. HR is defined as $\frac{H-S}{H+S}$, where H and S correspond to the source counts in the hard and soft bands, respectively. Statistical errors on the measured X-ray counts and HR values were computed to 1σ using the Bayesian estimation of HRs described in Park et al. (2006). The calculated HR for each observation is provided in Table 1. Overall, the scatter in the HR of each source is constant to within 2σ across their respective epochs.

3.2. Emission Spectra

Analysis of the X-ray emission spectra for J1405+0415 and J1610+1811 was performed consistent with Snios et al. (2021). We used the on-source and background regions described in Section 3.1. Source and background emission spectra were extracted from each observation using the CIAO routine `specextract`, and the multiple epochs were coadded with the `combine_spectra` task.

We analyzed the extracted spectra using CIAO's modeling and fitting package Sherpa. Each source and background spectrum, including the coadded data, was binned at 1 count per bin over the 0.5–7.0 keV band and fit using WStat statistics. We utilized a power-law model for the spectra that include both Galactic and intrinsic absorption effects [i.e., `phabs` $\cdot$ (`zphabs` $\cdot$ `powerlaw`)]. The Galactic hydrogen column density N_H was fixed to extrapolated values from Dickey & Lockman (1990) of $2.17 \times 10^{20}\,\mathrm{cm}^{-2}$ for J1405+0415 and $3.62 \times 10^{20}\,\mathrm{cm}^{-2}$ for J1610+1811. The photon index Γ ($dN/dE \propto E^{-\Gamma}$), intrinsic absorption column density, and the power-law normalization were allowed to vary for all models. The best-fit results from our spectral analysis are shown in Table 2, where the upper limits on N_H^i are reported at the 3σ level. The coadded spectra and model fits for J1405+0415 and J1610+1811 are shown in Figure 2.

In addition, we assessed each spectrum for the presence of emission lines. We defined an additional spectral model component of a Gaussian emission line (i.e., `zgauss`), and we performed a likelihood ratio test for each spectrum with the new model component. We defined a p value less than 0.001 as the detection threshold for a line feature in the emission spectrum. However, our analysis did not detect any line feature (s) at a $p < 0.30$ significance from any individual observation or coadded spectrum. Our lack of emission line detection from these two quasars is consistent with the spectral analysis of Snios et al. (2021).

Using best-fit spectral models, we measured the observed Galactic absorption-corrected flux for each spectrum. We measured the flux over the 0.5–7.0, 0.5–2.0, and 2.0–7.0 keV bands in order to investigate possible variations in soft or hard X-ray bands. The rest-frame 2–10 keV luminosity $L_{2-10\,\mathrm{keV}}$ was also calculated with each best-fit model. An aperture correction was applied to all measured fluxes and luminosities, where the correction factor was derived from the encircled counts fraction of the source region. We found a correction factor of 1.071 for J1405+0415 and 1.057 for J1610+0811. The measured X-ray fluxes and luminosities of our sources are shown in Table 2. We note that the flux of J1610+1811 is observed to vary across all bands at a $>3\sigma$ threshold, which is discussed further in Section 6.

Table 2
X-Ray Properties of the Quasar AGN

Object (1)	ObsID (2)	$C_{\rm obs}$ (3)	$N_{\rm H}^{i}$ (4)	Γ (5)	$f_{0.5\text{--}7.0\,\rm keV}$ (6)	$f_{0.5\text{--}2.0\,\rm keV}$ (7)	$f_{2.0\text{--}7.0\,\rm keV}$ (8)	$L_{2\text{--}10\,\rm keV}$ (9)	stat/dof (10)
J1405+0415	20408	281.8	<7.8	$1.48^{+0.12}_{-0.11}$	$35.4^{+2.4}_{-2.3}$	$12.4^{+1.1}_{-1.1}$	$22.8^{+2.4}_{-2.0}$	$13.9^{+2.3}_{-2.0}$	135.7/163
...	23649	393.7	<16.0	$1.63^{+0.17}_{-0.15}$	$34.6^{+2.3}_{-2.4}$	$12.3^{+1.6}_{-1.3}$	$22.1^{+1.9}_{-1.8}$	$15.2^{+3.0}_{-2.5}$	178.2/204
...	24316	362.8	<12.5	$1.46^{+0.12}_{-0.10}$	$35.7^{+2.2}_{-1.9}$	$12.3^{+1.2}_{-1.1}$	$23.5^{+2.1}_{-1.7}$	$13.8^{+2.2}_{-1.7}$	169.3/203
...	24317	616.6	$5.1^{+3.8}_{-3.5}$	$1.69^{+0.14}_{-0.13}$	$33.3^{+1.7}_{-2.0}$	$11.2^{+1.2}_{-1.1}$	$21.8^{+1.3}_{-1.3}$	$15.2^{+2.3}_{-2.2}$	234.6/245
...	25011	473.7	<9.2	$1.71^{+0.10}_{-0.09}$	$33.0^{+1.6}_{-1.8}$	$13.7^{+1.1}_{-1.1}$	$19.2^{+1.5}_{-1.5}$	$15.3^{+1.8}_{-1.7}$	194.1/222
...	25014	351.6	$9.2^{+6.2}_{-5.3}$	$1.83^{+0.20}_{-0.19}$	$32.8^{+2.6}_{-2.3}$	$11.2^{+1.5}_{-1.2}$	$22.2^{+2.0}_{-2.1}$	$16.4^{+3.5}_{-3.0}$	165.5/183
...	coadded	2476.5	$1.4^{+1.3}_{-1.3}$	$1.61^{+0.06}_{-0.06}$	$34.8^{+1.0}_{-1.0}$	$12.8^{+0.6}_{-0.6}$	$21.9^{+0.7}_{-0.7}$	$15.0^{+1.1}_{-1.0}$	394.9/386
J1610+1811	20410	392.8	<8.5	$1.72^{+0.15}_{-0.14}$	$49.6^{+3.0}_{-3.0}$	$19.5^{+2.0}_{-1.6}$	$29.8^{+2.8}_{-2.6}$	$21.7^{+3.6}_{-3.1}$	116.4/199
...	23648	628.5	$3.5^{+3.2}_{-3.0}$	$1.84^{+0.13}_{-0.13}$	$31.3^{+1.8}_{-1.9}$	$12.5^{+1.5}_{-1.2}$	$18.6^{+1.2}_{-1.2}$	$14.8^{+2.1}_{-2.0}$	214.2/249
...	24486	329.6	<15.7	$1.70^{+0.18}_{-0.17}$	$30.7^{+2.2}_{-2.2}$	$11.5^{+1.2}_{-1.4}$	$19.2^{+1.8}_{-1.6}$	$13.3^{+2.6}_{-2.3}$	154.4/170
...	24487	785.5	$5.3^{+2.7}_{-2.5}$	$2.02^{+0.12}_{-0.12}$	$35.4^{+1.8}_{-1.7}$	$15.1^{+1.5}_{-1.2}$	$20.3^{+1.1}_{-1.2}$	$18.5^{+2.2}_{-2.0}$	199.2/267
...	25035	360.7	<14.4	$1.83^{+0.18}_{-0.17}$	$32.3^{+2.7}_{-2.3}$	$13.1^{+1.7}_{-1.6}$	$19.3^{+1.8}_{-1.7}$	$15.2^{+3.1}_{-2.5}$	155.1/194
...	coadded	2493.3	$3.4^{+1.4}_{-1.3}$	$1.88^{+0.06}_{-0.06}$	$35.1^{+1.0}_{-1.0}$	$14.6^{+0.8}_{-0.7}$	$20.5^{+0.6}_{-0.7}$	$17.0^{+1.1}_{-1.1}$	305.8/369

Notes. (1) Object name. (2) Observation ID. (3) Background-subtracted counts over the 0.5–7.0 keV band from $1\farcs5$ radius circle centered on the quasar. (3) Spectral model. (4) Intrinsic column density, in units of 10^{22} cm^{-2}. Upper limits are reported at the 3σ level. (5) Photon index from 0.5–7.0 keV best-fit spectral model. (6) Observed 0.5–7.0 keV flux, in units of 10^{-14} erg cm^{-2} s^{-1}. (7) Observed 0.5–2.0 keV flux, in units of 10^{-14} erg cm^{-2} s^{-1}. (8) Observed 2.0–7.0 keV flux, in units of 10^{-14} erg cm^{-2} s^{-1}. (9) Rest-frame 2–10 keV luminosity, in units of 10^{45} erg s^{-1}. (10) Ratio of the final best-fit statistics to the degrees of freedom (dof).

4. Extended X-Ray Emission

4.1. Statistical Assessment of Morphology

Previous Chandra observations of J1405+0415 and J1610+0811 detected candidate X-ray jets coincident with radio features at projected distances of $2\farcs5$ and $6\farcs0$ from the AGN, respectively (Schwartz et al. 2020; Snios et al. 2021). At such small distance scales, care must be taken in accounting for the asymmetric PSF of Chandra when investigating for extended emission near the bright, point-source AGNs in our sample. We therefore applied a synthetic PSF comparison method for our analysis. This method is described in detail in Snios et al. (2021), and is briefly summarized here.

Simulations of 500 ray-tracing files for each X-ray observation were generated using the SAOsac ray-trace code, and the simulations were projected using MARX v5.5.1 with the ACIS Energy-Dependent Subpixel Event Repositioning algorithm. A spectral response for each simulation was defined using the extracted spectra from Section 3.2, and an aspect blur value of $0\farcs28$ was applied to each simulation. An annulus region was defined for each quasar that encompassed the observed radio features, and each annulus was divided into twelve 30° sectors. Consistent with Snios et al. (2021), we defined our coordinate system as 0° west rotating counter-clockwise. Given the possibility that extended X-ray features may lie in multiple sectors due to our definition method, we also assessed probabilities for the sum of adjacent sectors up to a total sector size of 90°.

The total counts for each annular sector were measured, and the simulated counts were scaled based on the ratio of the observed-to-simulated core counts. The average background counts per sector were determined using the background regions in Section 3.2. Under the assumption that the simulated and background count distributions per sector could be accurately modeled with Poisson statistics, we generated a predicted probability distribution per annular sector for each observation. Spatially coincident sectors were also coadded, as the sum of independent Poisson distributions is Poissonian

(Grimmett & Welsh 1986). Thus, we produced a coadded observation and a simulation for each quasar that included all relevant count statistics. We then compared the observed counts against the predicted probability distributions per sector, where we set a detection threshold probability of $p \leqslant 0.001$ for our analysis.

Based on our defined significance threshold, we detected extended X-ray emission in one sector per source at significance of $p < 0.0001$, or greater than 4σ. Images of the extended emission regions for J1405+0415 and J1610+0811 are shown in Figure 1, and our derived probabilities from the extended emission analysis are in Table 3. Our detection locations are consistent with the candidate jets determined by Schwartz et al. (2020) and Snios et al. (2021), while the detection threshold has increased from $\sim 3\sigma$ to $>4\sigma$. Furthermore, the extended X-ray emission is coincident with the known radio feature in each source, suggesting that the extended X-rays are due to jets. Physical properties of these X-ray features are discussed further in Section 5.

4.2. Deconvolved Images

In addition to our morphology analysis, we generated a deconvolved image of each quasar to image the extended X-ray emission. The deconvolved images were produced using the *arestore* task in CIAO, which applies the Richardson Lucy deconvolution algorithm to an image. Each observation was binned to the 0.5–7.0 keV band at a pixel size of $0\farcs25$, and we applied 100 iterations of the algorithm per observation. To avoid biasing from the known Chandra PSF artifact feature,[9] we used panda regions with an inner and outer radius of $0\farcs5$ and $1\farcs5$, respectively, to mask areas north of J1405+0415 and northeast of J1610+1811 prior to the deconvolution. Astrometric accuracy between the observations was verified using the cross-correlation method discussed in Section 2, and a coadded image of each quasar was subsequently generated.

---

[9] See the PSF artifact caveat in the CIAO User Guide: https://cxc.harvard.edu/ciao/caveats/psf_artifact.html.
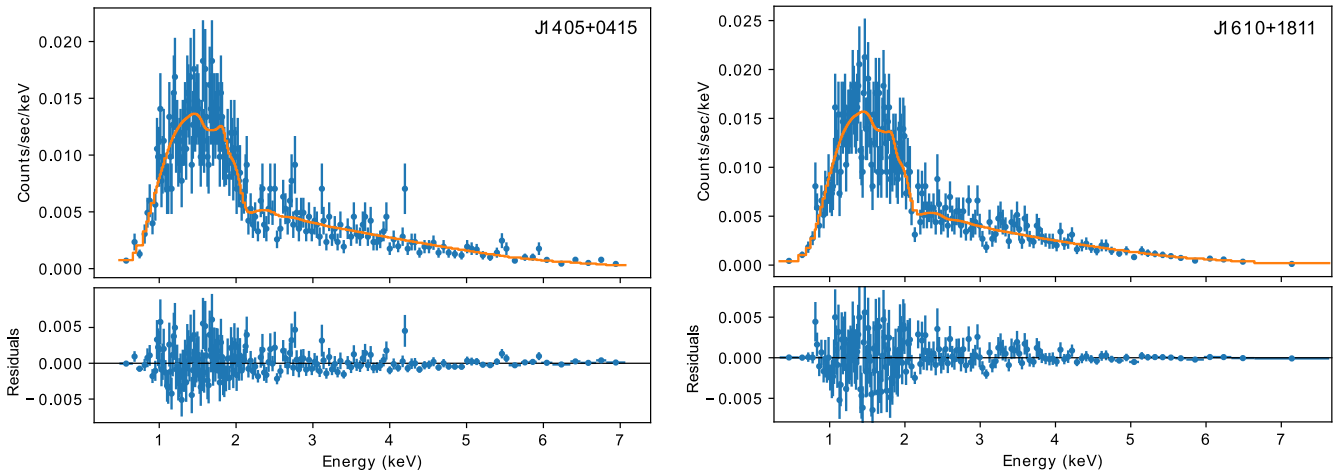
Figure 2. Chandra X-ray spectrum of J1405+0415 (left) and J1610+0811 (right). Each spectrum is binned by 10 counts per bin (solely for illustrative purposes) and is fitted over the 0.5–7.0 keV energy range with an absorbed power-law model with an intrinsic absorption component. The lower panel shows the residuals from the best-fit model.

Table 3
X-Ray Jet Morphological Analysis

Object (1)	r_{in} (2)	r_{out} (3)	C_{obs} (4)	C_{PSF} (5)	C_{bg} (6)	p (7)
J1405+0415	1.0	3.0	37	18.93	0.43	<0.0001
J1610+1811	2.0	6.0	27	6.30	1.88	<0.0001

Notes. (1) Object name. (2) Inner annular radius, in units of arcseconds. (3) Outer annular radius, in units of arcseconds. (4) Observed 0.5–7.0 keV counts. (5) Mean 0.5–7.0 keV counts from simulated PSF. (6) Expected background 0.5–7.0 keV counts. (7) Cumulative Poisson probability of detecting counts $\geqslant C_{obs}$. The results listed are sectors that satisfied our detection threshold of $p \leqslant 0.001$.

(This table is available in its entirety in machine-readable form.)

The resulting deconvolved images of J1405+0415 and J1610+1811 are shown in Figure 3. Examination of the images indicates excess X-ray emission in the same sectors as our morphology analysis of Section 4.1, and the enhancements are also spatially coincident with the radio features. Additionally, we observe an X-ray feature in J1610+1811 $\sim 1\rlap{.}''5$ northwest of the AGN that is parallel to the jet axis, though it is unclear if this is physical or a low-count artifact generated from the deconvolution process. Beyond this feature, we do not resolve any other extended structure in the deconvolved images. We also repeated the sector morphological analysis from Section 4 on the deconvolved images, and we did not detect any improvement in the statistical significance of any extended feature nor place constraints on the extended morphology. Overall, our interpretation of the deconvolved images for our quasar sample is complementary to our morphology analysis, though the limited quality of the deconvolved images reinforces the need for utilizing alternative methods in examining extended X-ray features with low count rates. Further analysis of these sources with a low-count image reconstruction algorithm may assist in resolving and characterizing the extended structure from these quasars (i.e., Stein et al. 2015; McKeough et al. 2016; Reddy et al. 2021), but such work is beyond the scope of this paper.

5. X-Ray Jet Flux and Surface Brightness

The X-ray flux and surface brightness of a jet can provide direct measurements of outflow power from an AGN as well as the evolution of the system (Marshall et al. 2002; Siemiginowska et al. 2002; Schwartz et al. 2006a, 2006b; Goodger et al. 2010; Snios et al. 2019a, 2019b). Thus, we measured the flux and the surface brightness of the X-ray features detected in Section 4. To begin, we attempted to identify edges of the extended X-rays using surface brightness profiles, but no edges were detected. We therefore assumed that the sector regions where extended X-rays were identified in Section 4 encompassed the total extended emission. Additionally, we assumed that the emission originated from the AGN and extended radially outward to the outer annular radius.

The HR of each X-ray jet was measured using the observed counts per sector C_{obs} with the HR derivation and background subtraction methods described in Section 3.1. The measured HR values for the source counts are $-0.46^{+0.13}_{-0.16}$ for J1405 +0415 and $0.02^{+0.20}_{-0.20}$ for J1610+1811, each of which is consistent within 2σ to the measured HR of their respective AGN. For completeness, we additionally measured the HRs of all remaining sectors to investigate for asymmetric HR trends from the system. We found the remaining sectors to have an average HR of $-0.28^{+0.16}_{-0.19}$ for J1405+0415 and $-0.21^{+0.09}_{-0.21}$ for J1610+1811, where each is consistent within 1σ to the extended X-ray sector and 2σ to the AGN. The consistency between our HR values is primarily due to the large errors on our measurements from the low-count statistics. Thus, longer exposures are required before HR variations in the extended X-ray emission of our quasar sample can be used for diagnostic purposes.

We account for the contribution of the quasar to the extended emission by subtracting the mean PSF simulated counts C_{PSF} from the total observed counts C_{obs}. We then modeled the emission using an absorbed power law (i.e., `phabs·power-law`). The spectral normalization was fixed equal to our measured X-ray jet count rates, and the Galactic hydrogen column density was fixed equal to the values used in Section 3.2. Since a spectrum of the extended X-ray emission could not be extracted for either quasar, we fixed the photon index to $\Gamma = 1.9$, which is consistent with the jet analysis of Snios et al. (2021). The observed 0.5–7.0 keV fluxes and rest-
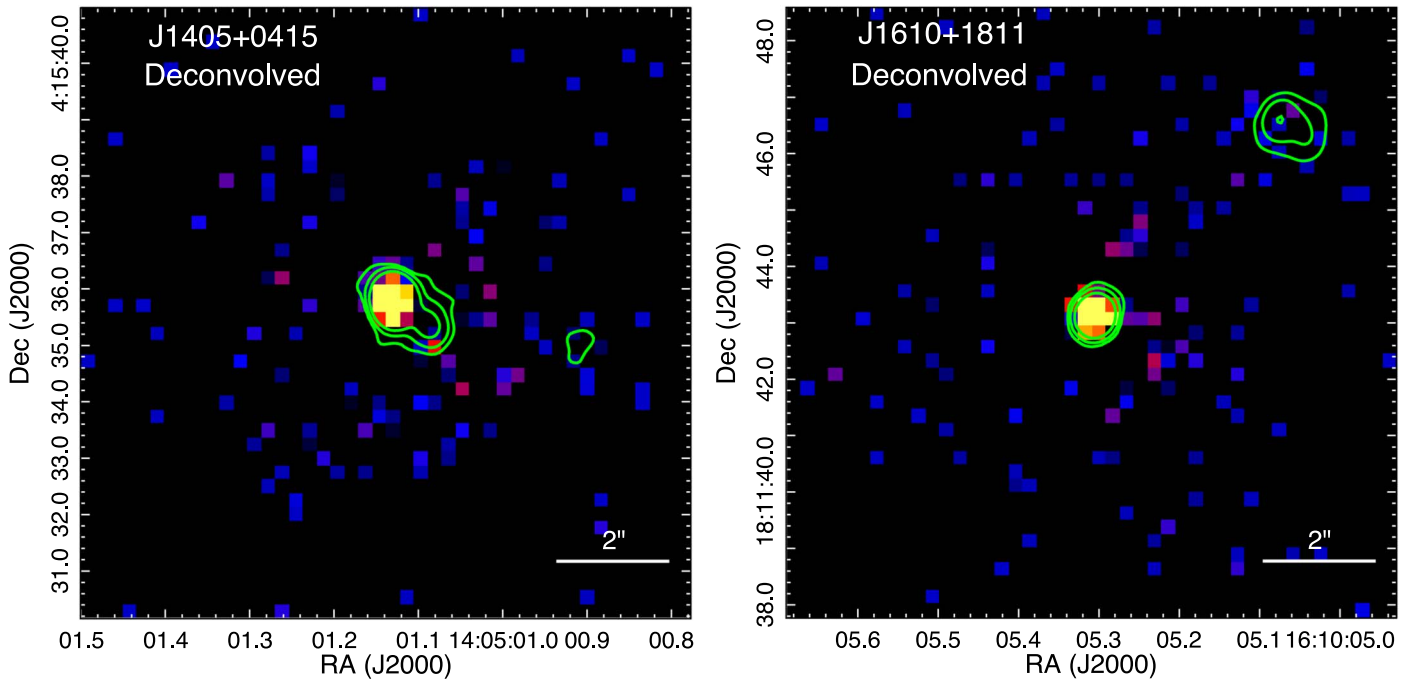
Figure 3. Deconvolved Chandra 0.5–7.0 keV images of the quasars J1405+0415 (left) and J1610+0811 (right). Each image is binned in 0″25 pixels and overlaid radio map contours (green) from VLA observed at 6.2 GHz. To avoid biasing in our analysis, we masked the nonphysical Chandra PSF artifact feature observed ∼1″ north of J1405+0415 and northeast of J1610+1811.

frame 2–10 keV luminosities of the jets, assuming no relativistic beaming, are provided in Table 4. We note that the luminosities of these two jets are low by an order of magnitude when compared with the five known resolved $z > 3.5$ X-ray jets (Worrall et al. 2020), extending X-ray high-redshift jet studies to a factor of ∼10 lower in X-ray power. Surface brightness was also calculated for each quasar, where we defined the width of the emitting region equal to 0″4, the FWHM of Chandra. The surface brightness measurements of the X-ray jets are provided in Table 4.

Comparing our flux measurements to the previous works on these sources (Schwartz et al. 2020; Snios et al. 2021), we found our fluxes to be lower than previous measurements by a factor of ∼2. However, we note that Snios et al. (2021) give jet flux measurement errors of a factor ∼2 as the number of jet counts in the 2018 observations were low. Thus, the flux measurements from our current study are broadly consistent with previous works for these sources, and our work leverages the follow-up Chandra observations to provide the most accurate X-ray measurements of these quasar systems to date.

Utilizing the jet and AGN fluxes from our analysis, we may additionally measure the jet-to-core flux ratio of each quasar, which may be used to discriminate between different emission mechanisms. For example, X-rays generated from inverse Compton upscattering of the cosmic microwave background radiation (IC/CMB) are theorized to increase the observed jet flux with increasing redshift, causing an elevated jet-to-core flux ratio for the distant quasar population (Schwartz et al. 2020). We therefore estimated the jet-to-core flux ratios f_{jet}/f_{core} for our high-redshift sources using the observed 0.5–7.0 keV fluxes in Tables 2 and 4. The ratio results are shown in Table 4, where both quasars possess a ratio of 0.7%. These results are consistent with the 1%–2% values measured for quasars at $z < 2$ (Marshall et al. (2018)). Our result also agrees with the f_{jet}/f_{core} measurements from the limited sample

Table 4
X-Ray Jet Properties

Object (1)	d_{jet} (2)	C_{src} (3)	f_{jet} (4)	S_{jet} (5)	L_{jet} (6)	f_{jet}/f_{core} (7)
J1405+0415	3.0	13.11	2.3	1.6	2.1	0.007
J1610+1811	6.0	18.82	2.6	0.9	2.2	0.007

Notes. (1) Object name. (2) Projected jet length, in units of arcseconds. (3) Source 0.5–7.0 keV counts from the jet. (4) Observed 0.5–7.0 keV jet flux, in units of 10^{-15} erg cm^{-2} s^{-1}. (5) Observed 0.5–7.0 keV jet surface brightness, in units of 10^{-15} erg cm^{-2} s^{-1} arcsec^{-2} (6) Rest-frame 2–10 keV jet luminosity, in units of 10^{44} erg s^{-1}. (7) Ratio of X-ray fluxes for the jet to core. All flux-related measurements assume 4π isotropic radiation and have an approximate factor of 2 uncertainty.

of quasars at $z > 3$ (Zhu et al. 2019; Worrall et al. 2020; Snios et al. 2021). Overall, our findings suggest that the jet-to-core flux ratio is redshift invariant for quasars at $z \lesssim 3.5$.

6. Brightness Variation in Core of J1610+1811

When reviewing the flux measurements from Section 3.2, a notable decrease in flux of ∼40% is observed from the core of J1610+1811 between the first X-ray observation (Observation ID (ObsID) 20410) in 2018 and observations made ∼3 yr later. In comparison, no change in flux is seen for J1405+0415 over the same time frame, disfavoring systematic causes for the changed flux from J1610+1811. Additionally, we examined other sources within the field of view of the J1610+1811 Chandra observations for flux changes and found no evidence of similar variability from any other source, further reinforcing that the observed J1610+1811 flux decrease is not systematic error. The model best-fit parameters for each observations of J1610+1811 agree within 1σ of one another, barring the normalization parameter that diverges by $>3\sigma$ between the

2018 and 2021 data sets. Furthermore, the decrease in the flux is $>3\sigma$ for both the soft (0.5–2.0 keV) and hard (2.0–7.0 keV) energy bands, as shown in Table 2. These properties of J1610+1811 merit further investigation.

We began our examination of J1610+1811 by searching for additional archival X-ray data of the source to understand its long-term flux activity. We located observations of the quasar with the X-ray Telescope (Burrows et al. 2005) on the Neil Gehrels Swift Observatory (Gehrels et al. 2004) that ranged from 2015 August 09–2017 October 18 with Target IDs 00033847, 00086042, and 00093242 (excluding ObsID 00086042012). Time-averaged source and background spectra were generated using the UK Swift Science Data Centre database (Evans et al. 2009), giving a total exposure of 11.1 ks. We fit the spectrum with a phabs·powerlaw model together with the method described in Section 3.2. From our analysis, we found a best-fit spectrum model with a photon index of $\Gamma = 1.56 \pm 0.19$ and fluxes $f_{0.5-7.0\,\mathrm{keV}} = (36.7^{+5.3}_{-4.3}) \times 10^{-14}\,\mathrm{erg\,cm^{-2}\,s^{-1}}$, $f_{0.5-2.0\,\mathrm{keV}} = (13.3^{+1.7}_{-1.8}) \times 10^{-14}\,\mathrm{erg\,cm^{-2}\,s^{-1}}$, and $f_{2.0-7.0\,\mathrm{keV}} = (22.9^{+5.4}_{-3.8}) \times 10^{-14}\,\mathrm{erg\,cm^{-2}\,s^{-1}}$. The measured Swift fluxes are consistent with the 2021 Chandra values, while the 2018 Chandra flux measurement remains elevated by at least 2σ across all examined energy bands. These results confirm that the core of J1610+1811 has undergone recent X-ray flux variability, where the elevated flux emission lasted for a maximum timescale of 3 yr.

A common explanation for brightness changes in quasars is the introduction of an intrinsic absorber traveling into the line of sight, which reduces the total observed flux (Markowitz et al. 2014). However, such an absorber preferentially obscures soft X-ray flux (rest-frame <2 keV), where an increasingly large column density is required in order to reduce the hard X-ray flux. The spectral X-ray properties of J1610+1811 strongly disfavor the explanation of a traveling intrinsic absorber as the column density of said absorber would be infeasibly large, exceeding Compton-thick levels of $1.5 \times 10^{24}\,\mathrm{cm^{-2}}$, to cause the observed decrease in hard X-ray flux for a quasar at $z = 3.122$. Such a drastic change in N_H^i would also have been easily detected with the absorbed power-law model utilized in Section 3.2, of which no apparent change in column density was observed.

Given the overall agreement in the spectral models for the different observations of J1610+1811, it is probable that the same primary emission mechanism is present in all data sets, albeit at differing emission rates. A period of flaring from the corona or an increase in the accretion rate of the AGN may explain the elevated X-ray emission from the source during the 2018 observation as a factor of $\sim$2 change is consistent with observations of other quasars (Petrucci et al. 2001; Fabian et al. 2015; Middei et al. 2019). Furthermore, the $1\farcs5$ radius extraction region used to measure the source's flux encompasses a projected distance of 11.4 kpc around the AGN, which is large enough to include X-ray emission from the jet and potential knotted structure within the jet. X-ray knots have been observed to flare in other radio galaxies, where the flux of a flaring knot can even exceed that of the AGN (e.g., Harris et al. 2006, 2009; Snios et al. 2019a). Thus, the observed fluctuations in brightness from the core of J1610+1811 may be explained as flaring from either the AGN or the inner jet region. In lieu of flaring from the knots, we expect the X-ray flux from the core to be dominated by activity from the corona and/or the AGN.

Flaring events may also be observed in other wavelength bands, though we were unable to locate multiwavelength data of the source over the desired time period. Multiwavelength monitoring of J1610+1811 is required to verify if the system is indeed currently in simple decline from a period of elevated emission activity. At present, also taking into account data from the Swift mission, we can only conclude consistency with a decline from flaring activity in 2017 and 2018.

7. Conclusions

We analyzed Chandra X-ray observations of the radio-loud quasars J1405+0415 and J1610+1811 at redshifts $z = 3.215$ and $z = 3.122$, respectively, for evidence of extended X-rays indicative of jets. Each source was observed for a total of 95 ks, and we successfully detected each quasar in the 0.5–7.0 keV band. HRs and emission spectra of the quasars were measured, and X-ray fluxes and luminosities were determined from the resulting spectral best-fits. We performed a morphological analysis of each X-ray source consistent with the method described in Snios et al. (2021), and extended X-ray features were detected in each system at a greater than 4σ threshold. The extended X-rays in each source are spatially coincident with existing radio features, which is consistent with our interpretation that the extended emission is generated via jets in these high-redshift quasars.

Observed fluxes and rest-frame luminosities of the X-ray jets were estimated for the two quasars, and their X-ray jet-to-core flux ratios were measured. In each system we found a jet-to-core flux ratio of 0.7%, which agrees well with ratio measurements from low-redshift quasars. The overall consistency of jet power relative to the AGN across a broad redshift range suggests that the X-ray jet emission mechanisms are independent of redshift, which disfavors theorized redshift dependent mechanisms like inverse Compton upscattering of the cosmic microwave background radiation (IC/CMB).

In addition to our morphological analysis, we detected a decrease in the observed 0.5–7.0 keV flux from the AGN of J1610+1811 between the 2018 and 2021 data sets. We confirmed that the decrease was at a $>3\sigma$ threshold, and the variation was observed across the both the soft (0.5–2.0 keV) and hard (2.0–7.0 keV) energy bands. Examination of archival Swift observations confirmed that the system increased in brightness between the years 2017 and 2018. We examined the observed physical properties for this phenomenon and concluded that flaring activity from the core between the years 2017 and 2018 is the most probable cause for the observed flux variations.

Overall, our results demonstrate the strength of the morphological analysis methods described in Schwartz et al. (2020) and Snios et al. (2021), which utilized "snapshot" surveys of high-redshift quasars to determine ideal candidates for follow-up extended emission studies, such as those in this article. Additionally, our work reinforces the benefits of utilizing high-resolution X-ray imaging in studying high-redshift quasars. High-resolution imaging should therefore continue to be a priority for both current and future X-ray missions that are intent on studying the evolution of our universe.

ORCID iDs

Bradford Snios ● https://orcid.org/0000-0002-4900-928X
Daniel A. Schwartz ● https://orcid.org/0000-0001-8252-4753
Aneta Siemiginowska ● https://orcid.org/0000-0002-0905-7375
Małgosia Sobolewska ● https://orcid.org/0000-0002-6286-0159
Mark Birkinshaw ● https://orcid.org/0000-0002-1858-277X
C. C. Cheung ● https://orcid.org/0000-0002-4377-0174
Herman L. Marshall ● https://orcid.org/0000-0002-6492-1293
Giulia Migliori ● https://orcid.org/0000-0003-0216-8053
Diana M. Worrall ● https://orcid.org/0000-0002-1516-0336

References

Bañados, E., Carilli, C., Walter, F., et al. 2018, ApJL, 861, L14
Bañados, E., Mazzucchelli, C., Momjian, E., et al. 2021, ApJ, 909, 80
Begelman, M. C., Blandford, R. D., & Rees, M. J. 1984, RvMP, 56, 255
Bîrzan, L., Rafferty, D. A., McNamara, B. R., Wise, M. W., & Nulsen, P. E. J. 2004, ApJ, 607, 800
Blandford, R. D., & Rees, M. J. 1974, MNRAS, 169, 395
Bridle, A. H., & Perley, R. A. 1984, ARA&A, 22, 319
Burrows, D. N., Hill, J. E., Nousek, J. A., et al. 2005, SSR, 120, 165
Cheung, C. C., Stawarz, Ł., & Siemiginowska, A. 2006, ApJ, 650, 679
Cheung, C. C., Stawarz, Ł., Siemiginowska, A., et al. 2012, ApJL, 756, L20
Dermer, C. D., & Atoyan, A. M. 2002, ApJL, 568, L81
Dickey, J. M., & Lockman, F. J. 1990, ARA&A, 28, 215
Evans, P. A., Beardmore, A. P., Page, K. L., et al. 2009, MNRAS, 397, 1177
Fabian, A. C., Lohfink, A., Kara, E., et al. 2015, MNRAS, 451, 4375
Freeman, P., Doe, S., & Siemiginowska, A. 2001, Proc. SPIE, 4477, 76
Fruscione, A., McDowell, J. C., Allen, G. E., et al. 2006, Proc. SPIE, 6270, 62701V
Gehrels, N., Chincarini, G., Giommi, P., et al. 2004, ApJ, 611, 1005
Gobeille, D. B., Wardle, J. F. C., & Cheung, C. C. 2014, arXiv:1406.4797
Goodger, J. L., Hardcastle, M. J., Croston, J. H., et al. 2010, ApJ, 708, 675
Grimmett, G., & Welsh, D. 1986, Probability: An Introduction (Oxford: Oxford Science Publications)
Harris, D. E., Cheung, C. C., Biretta, J. A., et al. 2006, ApJ, 640, 211
Harris, D. E., Cheung, C. C., Stawarz, L., Biretta, J. A., & Perlman, E. S. 2009, ApJ, 699, 305
Harris, D. E., & Krawczynski, H. 2002, ApJ, 565, 244
Heavens, A. F., & Meisenheimer, K. 1987, MRNAS, 225, 335
Ighina, L., Moretti, A., Tavecchio, F., et al. 2022, A&A, 659, A93
Markowitz, A. G., Krumpe, M., & Nikutta, R. 2014, MNRAS, 439, 1403
Marshall, H. L., Miller, B. P., Davis, D. S., et al. 2002, ApJ, 564, 683
Marshall, H. L., Gelbord, J. M., Worrall, D. M., et al. 2018, ApJ, 856, 66
McKeough, K., Siemiginowska, A., Cheung, C. C., et al. 2016, ApJ, 833, 123
McNamara, B. R., & Nulsen, P. E. J. 2012, NJPh, 14, 055023
Middei, R., Bianchi, S., Marinucci, A., et al. 2019, A&A, 630, A131
Pâris, I., Petitjean, P., Aubourg, E., et al. 2018, A&A, 613, A51
Park, T., Kashyap, V. L., Siemiginowska, A., et al. 2006, ApJ, 652, 610
Petrucci, P. O., Haardt, F., Maraschi, L., et al. 2001, ApJ, 556, 716
Planck Collaboration, Ade, P. A. R., Aghanim, N., et al. 2016, A&A, 594, A13
Reddy, K., Georganopoulos, M., & Meyer, E. T. 2021, ApJS, 253, 37
Schwartz, D. A., Marshall, H. L., Lovell, J. E. J., et al. 2006a, ApJL, 647, L107
Schwartz, D. A., Marshall, H. L., Lovell, J. E. J., et al. 2006b, ApJ, 640, 592
Schwartz, D. A., Siemiginowska, A., Snios, B., et al. 2020, ApJ, 904, 57
Siemiginowska, A., Bechtold, J., Aldcroft, T. L., et al. 2002, ApJ, 570, 543
Siemiginowska, A., Smith, R. K., Aldcroft, T. L., et al. 2003, ApJL, 598, L15
Simionescu, A., Stawarz, Ł., et al. 2016, ApJL, 816, L15
Snios, B., Nulsen, P. E. J., Kraft, R. P., et al. 2019a, ApJ, 879, 8
Snios, B., Nulsen, P. E. J., Wise, M. W., et al. 2018, ApJ, 855, 71
Snios, B., Wykes, S., Nulsen, P. E. J., et al. 2019b, ApJ, 871, 248
Snios, B., Schwartz, D. A., Siemiginowska, A., et al. 2021, ApJ, 914, 130
Sowards-Emmerd, D., Romani, R. W., Michelson, P. F., Healey, S. E., & Nolan, P. L. 2005, ApJ, 626, 95
Stein, N. M., van Dyk, D. A., Kashyap, V. L., & Siemiginowska, A. 2015, ApJ, 813, 66
Virtanen, P., Gommers, R., Oliphant, T. E., et al. 2020, NatMe, 17, 261
Worrall, D. M., Birkinshaw, M., Marshall, H. L., et al. 2020, MNRAS, 497, 988
Zhu, S. F., Brandt, W. N., Wu, J., Garmire, G. P., & Miller, B. P. 2019, MNRAS, 482, 2016